Supplementary Figures:

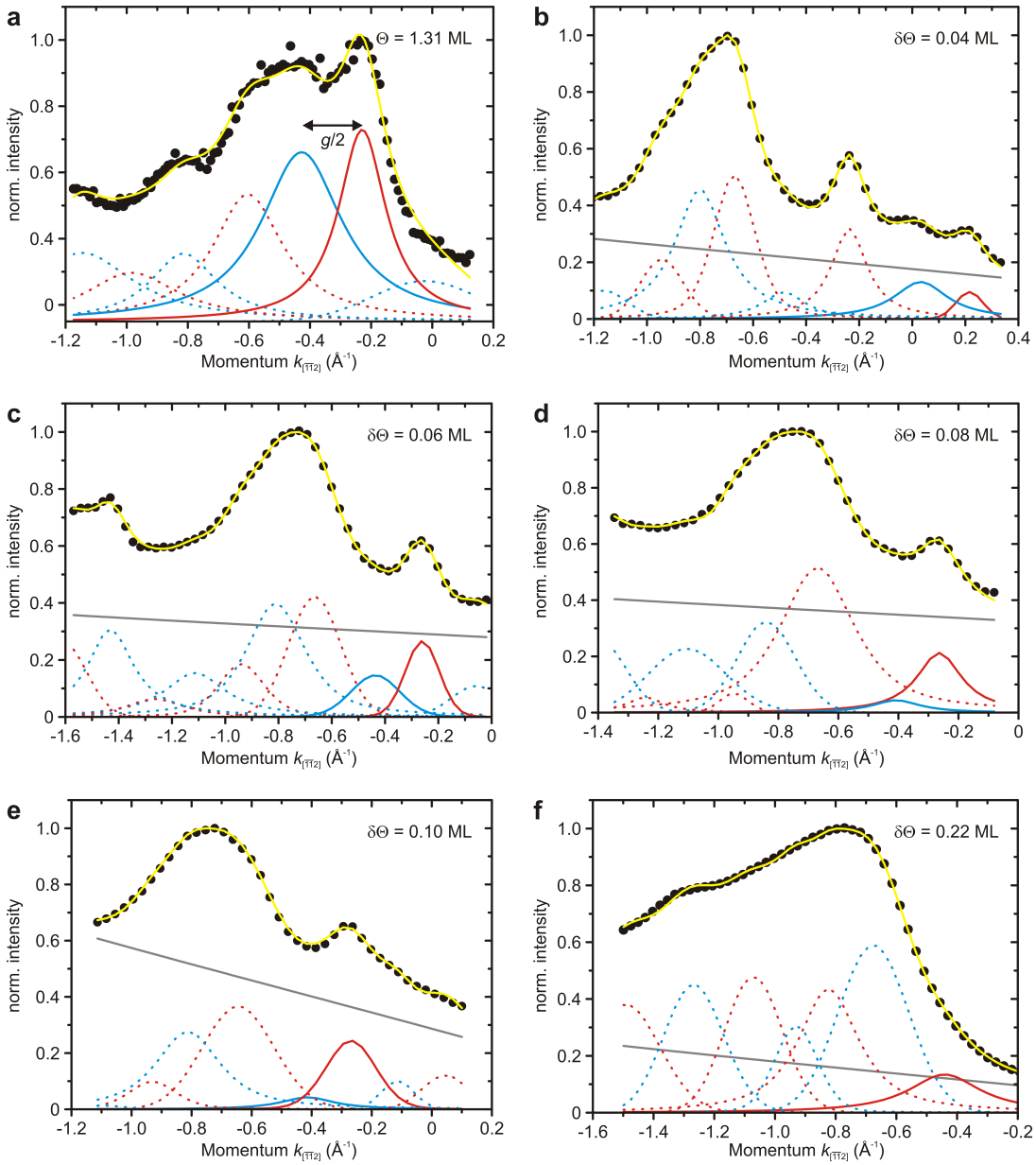

Supplementary Figure 1. **Spin-resolved MDCs along the $[\bar{1}\bar{1}2]$ direction for various amounts of excess Pb coverages.** **(a)** 0 ML, **(b)** 0.04 ML, **(c)** 0.06 ML, **(d)** 0.08 ML, **(e)** 0.1 ML, and **(f)** 0.22 ML. Points represent the experimental data. The solid (yellow) line is the total fit composed of subpeaks shown in the bottom. The blue and red color denotes the spin texture of these peaks deduced from the S_x-spin component shown in Fig.3a. Please note, the peaks located at the very end of the spectra may not exactly lie on the expected positions and are used more in order to stabilize the fit for the inner ones.

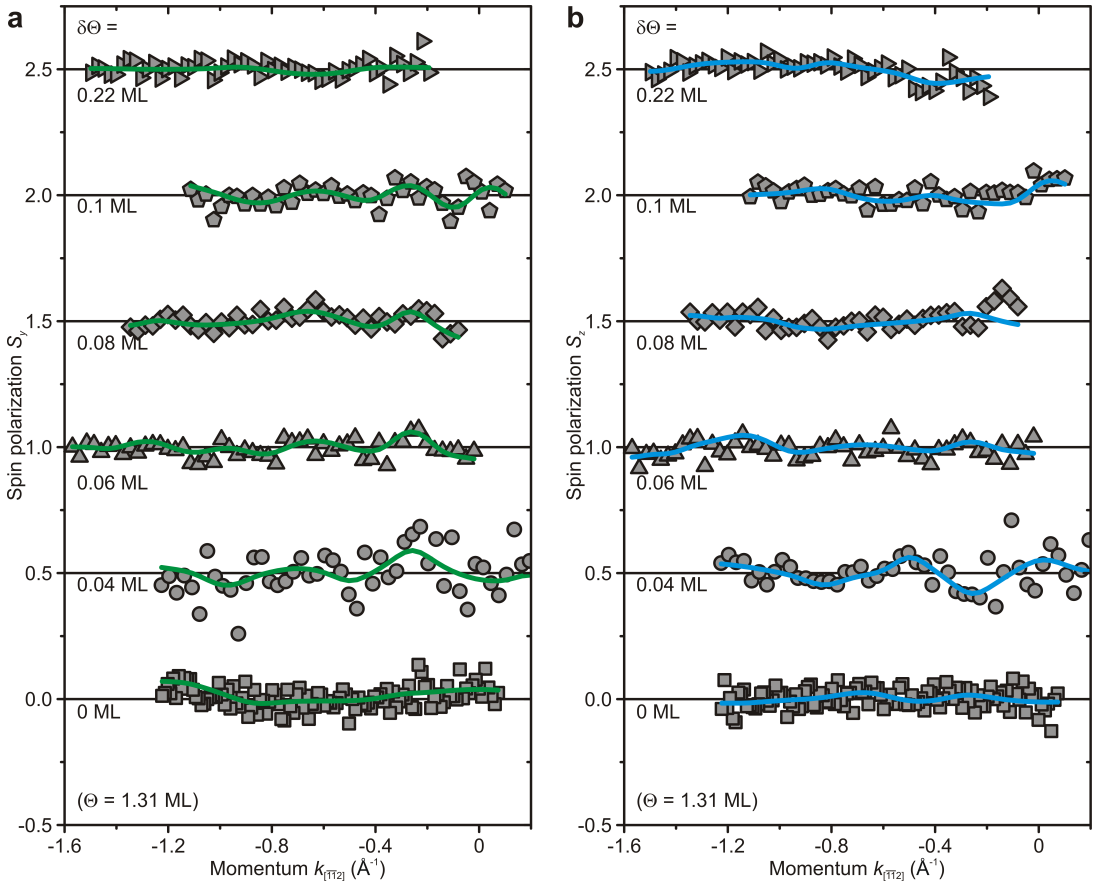

Supplementary Figure 2. **Spin polarization curves.(a)** and **(b)** show the S_y- and S_z-components of the photo-emitted electrons taken at E_F -50 meV along the $[\bar{1}\bar{1}2]$ direction.

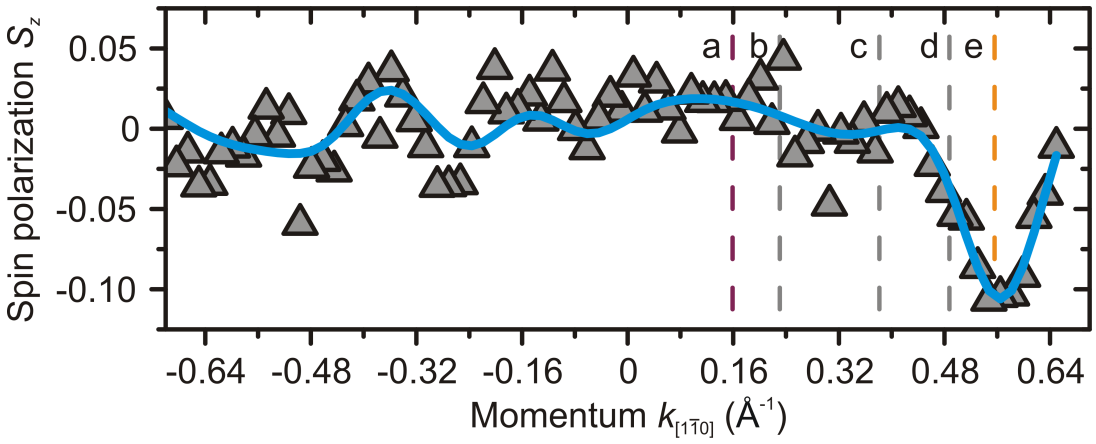

Supplementary Figure 3. **S_z-component of the electronic states at Fermi (E_F-50 meV) along the $[1\bar{1}0]$ direction.** In context of Fig.4a it is important to note that the z-component of the state at $k \approx 0$ does not contribute to the spin vector.

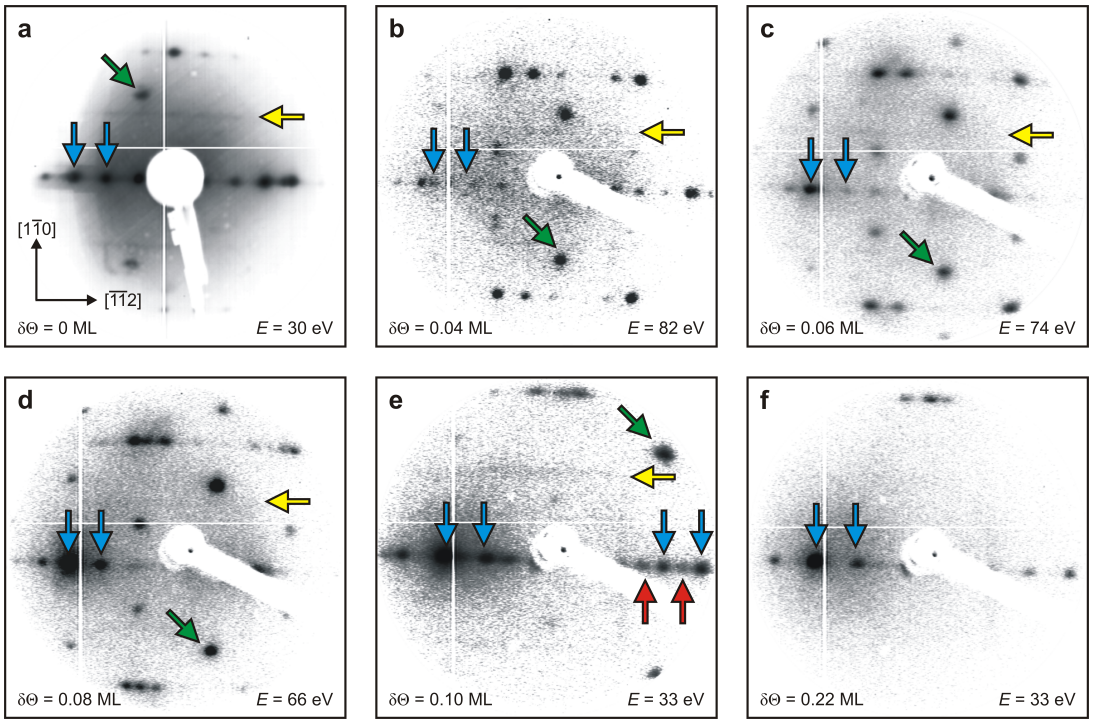

Supplementary Figure 4. **Optical LEED pattern of the 1.31 ML Pb/Si(557) phase with various $\delta\Theta$.** The arrows indicate characteristic features, blue: spot splitting of the (223) facet; yellow: $\times 2$ reconstruction from step sites; green: $\sqrt{3}$-reconstructions. The red arrows at $\delta\Theta = 0.1$ ML highlight the doubling of the period due to decoration of next but one terrace sites.

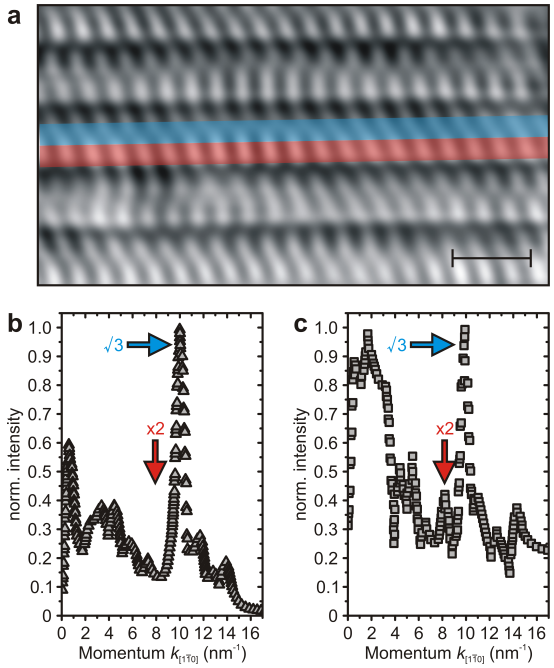

Supplementary Figure 5. **High resolution STM of Pb/Si(557). (a)** STM image taken at +1 V bias voltage (scale bar is 2 nm, T=50 K). **(b)** and **(c)** show normalized Fourier spectra taken in the center of a terrace (cf. bluish area in **(a)**) and at the step edges (cf. reddish area in **(a)**). The Fourier coefficients corresponding to step dimers and $\sqrt{3}$ wavelengths are marked by arrows. The $\times 2$ component at $k = 2\pi(2 \times 0.384\,\mathrm{nm}) = 8.18\,\mathrm{nm}^{-1}$ is seen only in spectra taken at the front side of the terrace. The most intense peak at $10.5\,\mathrm{nm}^{-1}$ stems from the $\sqrt{3} \times \sqrt{3}$ reconstruction.

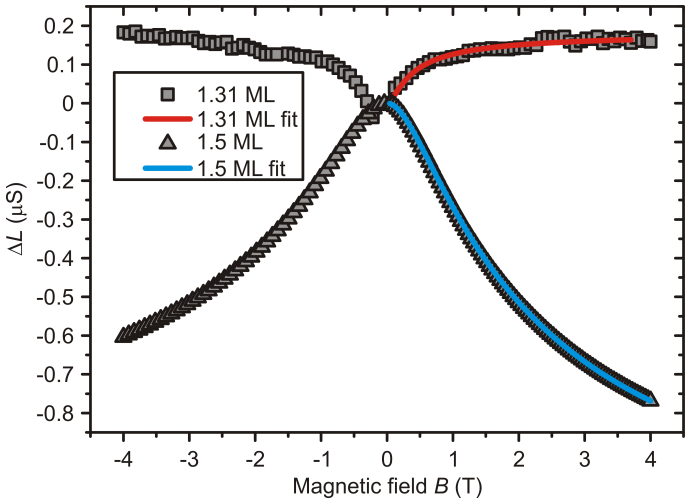

Supplementary Figure 6. **Magnetotransport measured along the wires.** Magneto transport data shown along to the chain directions for 1.31 ML (taken at 40 K) and 1.5 ML (50 K), respectively. The solid lines are a fit to experimental data according Hikami theory. The different signs in the change of ΔL directly reflect the difference of τ_{SO} for the 1.31 ML and 1.5 ML case (τ_0 and τ_{i} are almost identical).

SUPPLEMENTARY NOTE 1: SPIN POLARIZED ARPES MEASUREMENTS

The COPHEE beamline at Swiss Light Source allows the detection of a three-dimensional spin polarization vector of an electronic state in combination with its energy vs. momentum dispersion. The 6-axis manipulator has an angular precision of 0.05° over a large angular range and assesses temperature down to 10 K. Samples can be transferred into UHV by a fast load lock and can temporarily be stored under UHV conditions. The end station contains all typical surface science techniques, among others also LEED which has been used to check the sample preparation as well as to control the amount of excess coverage (see below). The sample size was $10 \times 5\ \mathrm{mm}^2$ and heated by direct current. The temperature was controlled with an infrared pyrometer. The 1.31 ML Pb phases on Si(557) were grown by deposition of 3 ML of Pb at 600 K and 2 monolayers (ML) at 570 K. The spectrometer is equipped with two orthogonal placed classical Mott detectors, allowing the simultaneous detection of all three spatial components of the spin expectation value as well as the momentum distribution curves revealing in total four independent data sets. The difference (asymmetry) of electrons backscattered elastically into two opposite detectors is transferred into a spin polarization by means of the Sherman function [1]. The arrangement of 8 detectors in total allows finally to extract the full spin polarization vector $\mathbf{S}$=(S_x, S_y, S_z).

In the spin-resolved mode the energy and angular resolution are 80 meV and 0.75° respectively, whereas 25 meV and 0.3° can be reached without spin resolution. In our case the spin integrated data have been taken with 2 eV pass energy (2 mm slits), the spin-resolved measurements were performed with 3 eV pass energy and a slit width of 6 mm. Despite the higher transmissions at these spectrometer conditions the integration time per data point was still around 180 s, i.e. the total time including the rotations of the sample for an entire Mott-MDC like those shown in Supplementary Figure 1 was in the range of 8 hours. From separate measurements done before performed in smaller k-range we know that spin texture has not changed upon adsorption from the residual gas (the pressure during the Mott measurements was 1×10^{-8} Pa.) While for excess coverages up to 0.1 ML Pb the overall structure of the Mott-MDCs is preserved, a pronounced change of structure is seen for 0.22 ML.

The original MDCs measured with the Mott detector are shown in Supplementary Figure 1 for various amounts of Pb excess coverages. The solid (yellow) line is a fit to the experimental data composed of many Pseudo-Voigt-type functions (and a linearly varying background). The color of these subpeaks (blue,red) refer to the spin texture, in this case solely of the S_x-component (see below). As obvious, the spin texture is alternating and equidistant supporting our conclusions [2]. The splitting of $\Delta k = g/2 = 0.2\ \mathrm{\AA}^{-1}$ is expected for antiferromagnetically coupled wires in this SODW-phase. Please note, the condition that the spin-texture of the subpeaks shown in the MDC must agree with the spin-components (shown in Fig. 3a for S_x and Supplementary Figure 2 for S_y and S_z) makes the fit very strict and reliable. For more information on the analysis method the reader is referred to Ref. [1].

The spin texture deduced form this analysis is shown by the color coded peaks and circles in Fig. 1b and Fig. 2a, respectively. Due to the better resolution, spin-integrated MDCs have been used in Figs. 1b and 2a instead of the Mott-MDCs.

Supplementary Figure 3 shows the S_y- and S_z-components of the MDCs taken at E_F-50 meV along the $[\bar{1}\bar{1}2]$ direction for various excess Pb coverages. Virtually, these two components are almost zero, thus only S_x, i.e. the spin component along the wires ($[1\bar{1}0]$ direction) is relevant and has been discussed in the paper. Nonetheless, for sake of completeness, the small amplitudes were plotted in Fig. 3b.

In addition to the $[\bar{1}\bar{1}2]$ direction we have also analyzed the $[1\bar{1}0]$ direction. As obvious from Fig. 4c, the Fermi surface along the wires becomes extremely complex due to the replica bands of all $\overline{\Gamma}$-points. The S_z-component is shown in Supplementary Figure 3.

SUPPLEMENTARY NOTE 2: ATOMIC STRUCTURE OF PB/SI(557); LEED AND STM

The coverage of the perfect Pb phase as well as the excess coverage can be calibrated extremely accurately (within 0.001 ML) by means of the Devil's staircase phases reported first for Pb/Si(111) [3]. All details regarding the Pb-coverage dependence for Pb/Si(557) are reported elsewhere [4, 5].

Fig. 2b in the paper shows high resolution LEED data taken in Hannover. These phases were prepared in similar manner at the SLS and the quality of the structure was controlled and checked by optical LEED. A sequence for various excess coverages is shown in Supplementary Figure 4. Clearly visible is the step train of the (223) facet structure marked by blue arrows. The spot splitting of the (223) phase refers exactly to the interwire distance of 1.58 nm as also shown in the STM image (presented in Fig. 1a). Furthermore, the formation of the a dense $\sqrt{3} \times \sqrt{3}$ Pb-reconstruction is seen (green arrows, in agreement with STM) as well as the half order spots (yellow arrows) stemming from the dimerization of Si-atoms at the edges. As the excess coverage is increased the intensity at half-order positions gradually vanishes supporting our former conclusions that the step edges are predominantly covered. Close inspection of the $\sqrt{3}$-diffraction peaks shows also a spot splitting pointing towards to the formation of a regular network of domain walls along the wires ($[1\bar{1}0]$ direction). The splitting of 10 % surface Brillouin zone nicely coincides with the superimposed intensity modulation shown by STM line scans in Fig. 1a. Finally, for adsorption

of 0.1 ML (see Supplementary Figure 4e and Fig. 2b,c) the period along the $[\bar{1}\bar{1}2]$ direction is doubled as obvious from the additional diffraction spots in between the former (223) facet spots (marked by red arrows).

All these fingerprints presented above have been analyzed in detail with high resolution LEED partly shown now in Fig. 2c [4, 5] and also STM (variable temperature) (shown in Fig. 1a, Supplementary Figure 5). While details of the STM analyses will be published elsewhere we restricted ourselves to STM-data which supports our former atomic model. From the STM image and corresponding line scan provided in Fig. 1a it is obvious that (i) a (223) facet with a width of 1.58 nm is formed, (ii) the period along the $[1\bar{1}0]$ direction of 5.76 Å=$\sqrt{3} \times 3.84$ Å $\times \cos(30°)$ refers to that of the $\sqrt{3} \times \sqrt{3}$ Pb-reconstruction on the mini-(111) terraces, and (iii) the 10-fold periodicity deduced form the spot splitting in LEED is seen as an intensity modulation, similar to that shown in a prior publication [7].

For Pb/Si(111) STM images of high coverage Pb monolayer phases have been measured and compared with DFT simulations [6]. For the 4/3 ML phase on H_3 or T_4 positions only a single protrusion per $\sqrt{3} \times \sqrt{3}$ unit cell is seen at high positive bias voltages (+1.5 V) , i.e. also in our study we should be basically sensitive to the periodicity of the $\sqrt{3}$ unit cell. The preferential occupancy of H_3- and T_4-positions on both Si(111) and Si(557) has been recently confirmed by high resolution Raman spectroscopy. The results will be published soon.

The dimerization of the step edges can be seen best from Fourier transformations. Supplementary Figure 5 shows two Fourier spectra taken on the center of a terrace and the step edge. The latter reveal clearly a Fourier component which corresponds to 2×3.84 Å. Also, the superimposed modulation on this structure (shown by the line scan in Fig. 1c) shows up in the Fourier spectra at 1-2 nm^{-1}. Systematic investigations in particular at various tunneling conditions will reveal further details about the atomic structure in the near future.

We want to point out the structural similarities found also for Pb/Si(553) by Kopciuszyński et.al. [8]. From their STM analysis supplemented by DFT calculations the authors report also on densely-packed Pb structure. The periodicity of 3.56 Å found along the $[1\bar{1}0]$ direction is significantly lower compared to what we found for Pb/Si(557). Nonetheless, the local geometry proposed by DFT calculations is reminiscent of a $\sqrt{3}$ reconstruction. Furthermore, complex domain wall phases are reported giving also rise to long-range modulations (2.7 nm) along the wires. Small differences between their and our model might be caused by slightly different terrace widths between (553) and (223) facets as well as different bonding scenarios at the step edges. Albeit details regarding the local bondings remain open, the comparison of these studies shows that the incompressibility of the high coverage Pb phase is causing long-ranged modulations along the wires which causes, at least in the case of Pb/Si(557), new phases with intriguing properties.

SUPPLEMENTARY NOTE 3: SURFACE MAGNETOTRANSPORT MEASUREMENTS

Magnetotransport measurements have been performed in order to quantify the changes of the spin-order in the Pb wire system in greater detail by analyzing the elastic (τ_0) and spin-orbit scattering times (τ_{SO}). Therefore, low–doped Si(557) samples (15x15 mm^2 in size) with eight $TiSi_2$ contacts have been used. By laser cutting (the samples were protected with resist) in total four 5 mm long slits from the center of the edges towards the center of the sample were made in order to match the conditions for a modified Van der Pauw geometry. The electrical current passed across the sample can be geometrically adjusted by help of the additional contacts in order to maximize the sensitivity regarding the anisotropy so that current is either parallel or perpendicular to the step direction. The contacts were fabricated by evaporation of Ti on the HF-dipped samples in a vacuum of 10^{-4} Pa at elevated temperatures between 700 and 800 °C. Afterwards the samples were mounted on the sample holder and transferred into the main UHV-chamber (base pressure 1×10^{-8} Pa). Crystalline Si surfaces were obtained by subsequent heating the samples by electron bombardment to temperatures of 1100 °C. The morphology was controlled in detail by spot profile analysis (SPA) LEED.

Pb was evaporated out of a ceramic crucible and the amount was controlled by a quartz microbalance. Pb films in the monolayer regime were produced in a two-step process by first depositing 3 ML at 600 K and 2 ML at 570 K . This leaves behind a monolayer of Pb (1.31 ML, 1 ML=7.83×10^{14} cm^{-2}) on the Si substrate and restructures the surface into (223) facets. A precise measurement of the residual coverage by SPA-LEED is obtained by using the Pb/Si(557) phase diagram reported elsewhere [4]. In order to vary the film thickness from this well defined coverage, further minute amounts of Pb are evaporated onto the sample at low temperatures around 80 K and monitored by the quartz microbalance.

For magnetotransport measurements the prepared Pb–phases are transferred in–situ to the position of the magnet. The superconducting split coil magnet reaches magnetic fields of $\pm$ 4 T, which were directed perpendicular to the sample surface. Cooling of the samples during measurements was done by a cryostat with a temperature range of 4 K (with cooled radiation shield) to 300 K. The temperature is measured by a Si-diode mounted on the cryostat itself and was calibrated using dummy samples with thermocouples.

A quantitative description of spin–orbit interaction and magneto resistance was elaborated by Hikami and coworkers [9]. The

change of the magnetoconductance $\Delta L = L(B) - L(0)$ is given by

$$\Delta L(B) = -L_{00}\left[f\left(\frac{B_o + B_{so}}{B}\right) - \frac{3}{2}f\left(\frac{4/3B_{so} + B_i}{B}\right) + \frac{1}{2}f\left(\frac{B_i}{B}\right)\right] \tag{1}$$

with

$$f\left(B_\nu/B\right) = \Psi(1/2 + B_\nu/B) - ln(B_\nu/B), \tag{2}$$

where Ψ is the di-gamma function and $L_{00} = e^2/(2\pi^2\hbar)$. B denotes the externally applied magnetic field and the B_ν, ν = i,o,so are defined as $B_\nu = \hbar \cdot n/(4ev_{\rm F}^2\tau_{\rm o}\tau_\nu)$. Hence, for a given Fermi velocity $v_{\rm F}$ of the electrons with charge e in an n-dimensional system all essential scattering parameters $\tau_{\rm i}$ (inelastic), $\tau_{\rm o}$ (elastic), and $\tau_{\rm so}$ (spin–orbit) can be determined. For further details regarding experiments and the fits see Ref.[10].

Exemplarily, the data for the 1.31 ML and 1.5 ML Pb/Si(557) together with the Hikami-fits are shown in Supplementary Figure 6 for the direction along the wires ($[1\bar{1}0]$ direction). As obvious, the change of the conductance as a function of the magnetic field is fundamentally different for the two cases shown. The decrease of the conductance with increasing magnetic field in the case of 1.5 ML is a clear hint of an effective spin-orbit coupling. In contrast, for 1.31 ML where the step edges are not decorated, the opposite behavior is found. The detailed analysis of the magnetotransport data revealed in the latter case $\tau_{so} = 6 \times 10^{-12}$ s. For the 1.5 ML case the spin-orbit scattering time is around 10^{-14} s, i.e. two orders of magnitude lower. The elastic scattering times differ by only a factor of two ($\tau_{\rm o,1.31ML} = 1 \times 10^{-14}$ s, $\tau_{\rm o,1.5ML} = 2 \times 10^{-14}$ s). Further details can be found in Ref. [10]. The error of the scattering times is typically about 10-30 %.

SUPPLEMENTARY NOTE 4: SPIN DEPHASING TIME IN THE SODW STATE; THEORY

For the case of Fermi surface (FS) nesting between two spin-orbit coupled split bands with a wavevector $\mathbf{Q}$, a SODW Hamiltonian can be written in the Nambu-Gor'kov spinor $\Psi_{\boldsymbol{k}} = [\psi_{\boldsymbol{k}\uparrow}, \psi_{\boldsymbol{k}\downarrow}, \psi_{\boldsymbol{k}+\boldsymbol{Q}\uparrow}, \psi_{\boldsymbol{k}+\boldsymbol{Q},\downarrow}]^T$ as

$$H = \sum_{k,\sigma}\frac{k^2}{2m}\psi^\dagger_{k,\sigma}\psi_{k,\sigma} + \alpha_R k\sigma_y\psi^\dagger_{k,\sigma}\psi_{k,-\sigma} + \Delta\psi^\dagger_{k\sigma}\big(\sigma_x \otimes \sigma_z\big)\psi_{k+Q,-\sigma} + (k \to k+Q), \tag{3}$$

where k is crystal momentum (along the wire which is along x) and $\sigma = \pm$ is spin index of electron with mass m. σ_i are the 2×2 Pauli matrices. α_R is the Rashba-type spin-orbit coupling, and Δ is the SODW order parameter defined as [11]: $\Delta(\boldsymbol{k}) = gk\psi^\dagger_{\boldsymbol{k}+\boldsymbol{Q},\nu}[\sigma_z \otimes \sigma_x]_{\nu\nu'}\psi_{\boldsymbol{k},\nu'}$ with g being the contact Coulomb potential. The screened Coulomb potential scales with the size of the excess coverage as $g(r) = g(0)\exp(-qr)$, where q is is the screening parameter. Earlier self-consistent solution for SODW in 2D electron gas shows that the SODW order parameter scales in the same way as g on the excess coverage, implying $\Delta(r) = \Delta(0)\cdot\exp(-qr)$. This also leads to $S_x = \sum_{k,\sigma}\psi^\dagger_{k,\sigma}\sigma_x\psi_{k,\sigma} \to S_x(0)\cdot\exp(-qr) + \text{const.}$

By fitting to the experimental data, we get $S_x(0)$=0.56 and q=27.8 (in units of excess coverage ML).

In the presence of scattering, the spin dynamics can be described by the kinetic equation[12]

$$\frac{\partial\mathbf{S_k}}{\partial t} + \mathbf{S_k}\times\mathbf{\Omega_k} = \frac{\langle\mathbf{S_k}\rangle - \mathbf{S_k}}{\eta} + \mathbf{P}, \tag{4}$$

where $\mathbf{S_k}$ is the spin polarization vector, $\mathbf{P}$ is any external spin source, η is the scattering time. $\mathbf{\Omega_k}$ is the effective Larmor frequency defined for our case by $\mathbf{\Omega_k} = (\Omega_{\rm R}k_x/k_{\rm F}, 0, \Omega_{\rm SODW})$, where $\Omega_{\rm R} = 2\alpha_{\rm R}k_{\rm F}/\hbar$, and $\Omega_{\rm SODW} = 2\Delta/\hbar$ are the frequencies corresponding to Rashba-type SOC and SODW, respectively. In our case, $\mathbf{P}$=0, and the initial condition for the spin is $\mathbf{S_k}(0)_x$ (we ignore the other components of the spin polarization being negligibly small), we can solve the above equation analytically in the limit of $\Omega_{\rm R} < \Omega_{\rm SODW}$ on the FS, and get $S_x(t) = S_x(0)\cdot\exp(-t/\tau_{\rm so})$, where the spin dephasing time is

$$\tau_{\rm so} = \frac{1 + \sqrt{1 + \Omega^2_{\rm SODW}\eta^2}}{\Omega^2_{\rm R}\eta} + \text{const.} \tag{5}$$

Inserting the exponential dependence of the SODW gap on the excess coverage ML and keeping all other parameters constant, we get a good fit of the spin-depasing time τ with the experimental value for a realistic parameter set of SODW gap Δ= 20 meV, $\eta = 10^{-20}$ s and $\Omega_{\rm R}$=2.6 $\times 10^{12}$ Hz.

Supplementary References:

[1] Meier F., Dil J.H. & Osterwalder J. Measuring spin polarization vectors in angle-resolved photoemission spectroscopy. *New J. Phys.* **11**, 125008 (2009).

[2] Tegenkamp C., Lükermann D., Pfnür H., Slomski B., Landolt GH. & Dil J.H. Fermi nesting between atomic wires with strong spin-orbit coupling. *Phys. Rev. Lett.* **109**, 266401 (2012).

[3] Stepanovsky S., Yakes M., Yeh V. , Hupalo M. & Tringides M.C. The dense $\alpha\sqrt{3} \times \sqrt{3}$ Pb/Si(1 1 1) phase: A comprehensive STM and SPA-LEED study of ordering, phase transitions and interactions. *Surf. Sci.* **600**, 1417-1430 (2006).

[4] Czubanowski M., Schuster A., Akbari S., Pfnür H. & Tegenkamp C. Adsorbate induced refacetting: Pb chains on Si(557). *New J. Phys.* **9**, 338 (2007).

[5] Czubanowski M., Pfnür H. & Tegenkamp C. Atomic chain ordering with ultra-long periods: Pb/Si(557). *Surf. Sci.* **603**, L121-L124 (2009).

[6] Chan T.-C., Wang C.Z., Hupalo M., Tringides M.C. , Lu Z.-Y. & Ho K.M. First-principles studies of structures and stabilities of Pb/Si(111). *Phys. Rev. B* **68**, 045410 (2003).

[7] Tegenkamp C., Kallassy Z., Pfnür H., Günter H.-L., Zielasek V. & Henzler M. Switching Between One and Two Dimensions: Conductivity of Pb-induced Chain Structures on Si(557). *Phys. Rev. Lett* **95**, 176804 (2005).

[8] Kopciuszyński M., Dyniec P., Krawiec M., Łukasik P., Jalochowski M. & Zdyb R. Pb nanoribbons on the Si(553) surface. *Phys. Rev. B* **88**, 155431 (2013).

[9] Hikami S., Larkin A.I. & Nagaoka Y. Spin-Orbit Interaction and Magnetoresistance in the Two Dimensional Random System. *Prog. Theor. Phys.* **63**, 707-710 (1980).

[10] Lükermann D., Gauch M., Czubanowski M., Pfnür H.& Tegenkamp C. Magneto transport in anisotropic Pb films and monolayers. *Phys. Rev. B* **81**, 125429 (2010).

[11] Das T. Interaction Induced Staggered Spin-Orbit Order in Two-Dimensional Electron Gas. *Phys. Rev. Lett.* **109**, 246406 (2012).

[12] Tarasenko S.A. Scattering induced spin orientation and spin currents in gyrotropic structures. *JETP Lett.* **84**, 199-203 (2006).